ARTICLE

# Physical Chemistry of the Mn/ZnO (000$\bar{1}$) Interface Probed by Hard X-ray Photoelectron Spectroscopy

Mac C. Mugumaoderha,* Robert Sporken, Jacques Ghijsen, and Jacques A. Dumont

Research Centre in Physics of Matter and Radiation, University of Namur (FUNDP), Rue de Bruxelles 61, B-5000 Namur, Belgium

ABSTRACT: The oxidation of a thin Mn film grown on a ZnO (000$\bar{1}$) surface and the subsequent diffusion of Mn into the oxide single crystal are investigated in situ by using high-energy X-ray photoelectron spectroscopy (HAXPES). Using hard X-rays allows one not only to investigate the chemistry at the heterojunction but also to describe in detail the thermal diffusion process and the electron energy band alignment at the Mn/ZnO interface. Charge transfer occurs between the metallic Mn film and the ZnO surface which causes the ZnO valence band to bend downward in the interfacial region.

Annealing at 630 K leads to the formation of a thin two-dimensional MnO film which induces an upward bending of ZnO bands. Upon annealing at 800 K, Mn diffuses into the substrate crystal. A Mn concentration profile is derived, and a diffusion coefficient of 1.4×10^{-19} m^2/s is experimentally determined.
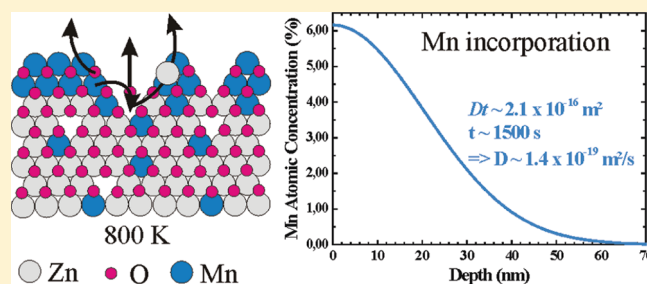
1. INTRODUCTION

Physical and chemical processes occurring at buried heterojunctions are a major issue of today's electronics. The nanometric downscaling of devices gives a new, unrivaled significance to interfacial processes regarding the efficiency of modern technologies. Buried interfaces are traditionally probed by destructive techniques such as depth profiling which can involve several artifacts such as preferential sputtering, sputter-induced segregation, ion implantation, or activation of interfacial reactions. New methods and means that allow probing buried interfacial processes while limiting sample damage induced by the measurement itself are now available. High-energy X-ray based techniques[1] and in particular bulk-sensitive hard X-ray photoelectron spectroscopy[2] are perfectly suited for such a task. In the present work, high-energy X-ray photoelectron spectroscopy (HAXPES) was used to probe interfacial reactions at the Mn/ZnO interface upon annealing.

Zinc oxide is a wide band gap oxide used in various industrial applications (as catalytic material, whitener, UV absorber) but is also a promising material for new technologies: the presence of a two-dimensional electron gas at ZnO/ZnMgO interfaces can be essential for future high-speed oxide electronics while (Zn,TM)O diluted magnetic oxides (DMOs), where TM is a transition metal, could be used as spin electrodes for room-temperature spintronic applications.[3,4] Achieving perfect control of the structure of these ZnO based ternary compounds is mandatory to establish the desired physical properties. A wide diversity of magnetic properties have been reported in the literature for (Zn,TM)O, indicating that the magnetization in such DMOs depends on the growth and doping conditions. Preparing structurally well-ordered ternary compounds still poses a challenge to the point that the experimental parameters and associated physical properties such as the magnetization of DMOs can hardly be reproduced by different groups.[5−7]

In the present work, we focus on the (Zn,Mn)O system. In order to understand the interaction between Mn and the ZnO host lattice, a not much reported route consists of studying the physics of the Mn/ZnO interface upon annealing. Using synchrotron radiation photoelectron spectroscopy, Zou et al.[8] and Guziewicz et al.[9] studied the electronic properties of Mn/ZnO (000$\bar{1}$) upon annealing. Zou et al. found that after annealing at a temperature of ~900 K interfacial reactions lead to Mn oxides involving Mn^{3+} or Mn^{4+}. The investigations of Guziewicz et al. focused on the contribution of Mn 3d states to the valence band of ZnMnO.

2. EXPERIMENTAL METHODS

The (000$\bar{1}$) O-terminated faces of ZnO single crystals produced by hydrothermal growth were polished by a mechanical and chemical method (NovaSiC). The samples were then cleaned for 10 min in an acetone ultrasonic bath and blown dry with nitrogen after the bath.

Next, they were loaded into ultrahigh-vacuum (UHV, base pressure below 2×10^{-9} hPa) at the beamline BW2 at DESY and cleaned in situ by several Ar$^+$ sputtering (1 keV, 5 min) and annealing (875 K, 30 min) cycles until no contaminants were seen by HAXPES and a sharp low energy electron spectroscopy (LEED) pattern of the unreconstructed surface was observed. The samples were heated by direct current flow across a glassy carbon plate in contact with the single crystal. The temperature was calibrated using a type-K thermocouple in contact with the ZnO surface before cleaning and Mn deposition. Mn was sublimated from a resistively heated filament coiled around a Mn pellet (99.999% purity) and with the samples very near room
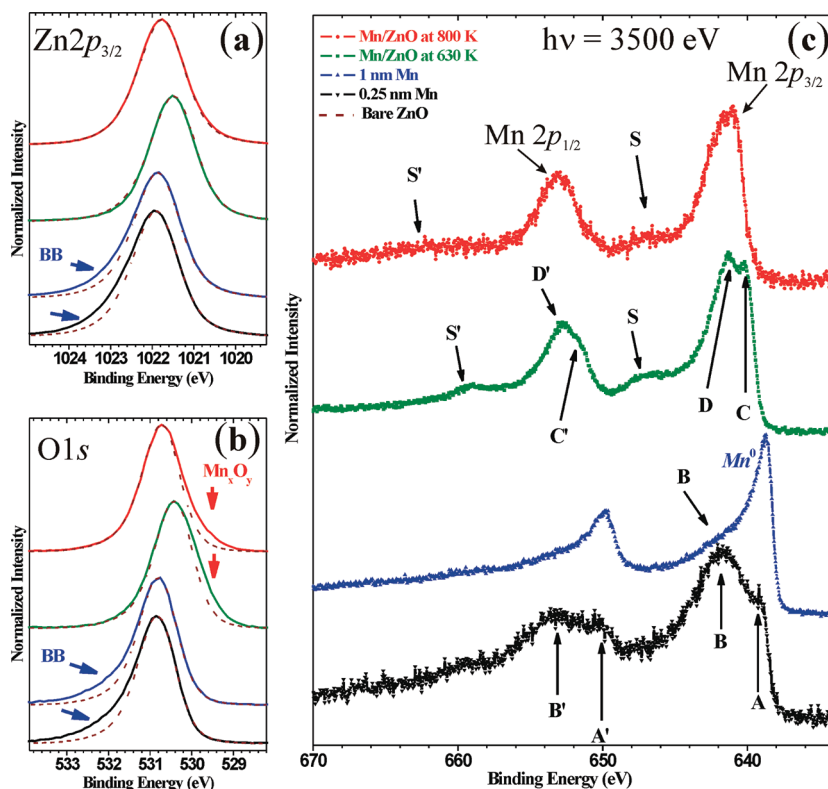
Figure 1. (a) Zn 2p$_{3/2}$, (b) O 1s, and (c) Mn 2p photoelectron spectra at different stages of the experiment: bare ZnO, 0.25 nm Mn deposition, 1 nm Mn deposition, and annealing at 630 and 800 K. Dotted lines are the bulk ZnO related spectra plotted for comparison. Labels and arrows are explained in detail in the text.

temperature (exposed to the radiative heat from the evaporator during 3 min of Mn deposition). The deposition rate measured using a quartz oscillator before each Mn growth ranged between 0.125 and 0.25 nm/min. Mn coverage is specified as equivalent thickness, that is, the thickness of a uniform layer of bulk Mn with the same mass. HAXPES spectra were recorded at a photon energy of 3500 eV with a total energy resolution of 0.5 eV. Photoelectrons were collected in the normal emission geometry at an angle of 45° with respect to the polarization direction of the beam. The electron binding-energy scale was calibrated relative to the 4f signal of a gold reference sample. The intensity of the Au 4f$_{7/2}$ reference spectra was also used to normalize the spectra to the incident photon flux.

3. RESULTS

3.1. Spectral Features. Figure 1 shows the Zn 2p, O 1s, and Mn 2p photoelectron spectra of the Mn/ZnO (000$\bar{1}$) system recorded at different stages of the experiment, which shall be discussed in the following sections.

Mn Deposition at Room Temperature. Both Zn 2p and O 1s peaks broaden asymmetrically (see feature BB at the high binding energy side in Figure 1) after deposition of Mn, which is attributed to the downward bending of the ZnO band structure close to the interface. Band bending at a metal/semiconductor heterojunction is a common feature caused by work function mismatch between the two materials. In the present case, electron transfer from Mn to ZnO is expected because Mn has a lower work function than ZnO (Mn: 4.1 eV vs ZnO: 4.1−5.3 eV[10−12]). The signature of band bending in conventional X-ray photoelectron spectroscopy (XPS) usually consists of a rigid shift

of the spectral lines from the semiconductor. In the present case, band bending results in an asymmetry in the semiconductor related line shapes. This is due to the much longer electron escape depth when using high energy X-rays: for example, in the case of O 1s, the inelastic mean free path (IMFP) is 4.6 nm when using $h\nu$ = 3500 eV and is reduced to 1.9 nm when using a typical Al Kα X-ray source ($h\nu$ = 1486 eV). In addition, the depletion region in wide band gap semiconductors can be strongly confined to the surface. As a result, although band bending occurs, photoemission spectra from the semiconductor can still be dominated by the bulk feature, as was shown by Sumiya et al. who studied GaN using a photon energy of 5.95 keV.[13]

The charge transfer between Mn and ZnO is confirmed by the shape of the Mn 2p lines at the earliest stages of the experiment. Indeed, upon deposition of 0.25 nm Mn, the Mn 2p spectrum reflects the superposition of two distinct contributions referred to as A and B in the spectrum. Components A and A′ are the low binding energy contributions to Mn 2p$_{3/2}$ and Mn 2p$_{1/2}$ signals and are related to metallic Mn, whereas components B and B′, at higher binding energy, indicate an electron transfer from Mn to the ZnO. This electron transfer is directly in relation with the downward bending of the ZnO bands mentioned above. When the Mn layer thickness is increased to 1 nm, the Mn 2p line shape is closer to that from metallic Mn. Nonetheless, the signal coming from the interfacial Mn layer (satellite B) remains visible.

Annealing Experiments. Annealing removes the asymmetric broadening at the high binding energy side for both the Zn 2p and O 1s lines, which are both shifted to a lower binding energy. These changes are again associated to band bending and explained in detail in section 3.3. In addition, a new feature

20604

dx.doi.org/10.1021/jp206075w |*J. Phys. Chem. C* 2011, 115, 20603–20609

appears at the low binding energy side of the O 1s line; which is attributed to the formation of manganese oxide. According to Oku et al.,[14] the photoemission spectral features of most Mn_xO_y compounds should appear close to 529.6 eV. Thus, the stoichiometry of Mn_xO_y cannot be elucidated based on the O 1s line shape alone.

Upon annealing the Mn/ZnO system at 630 K for 25 min, Mn is fully oxidized. Indeed, the main lines of Mn 2p shift to higher binding energy and satellites indicated by S and S′ in Figure 1 appear at 6.5 eV above them. These satellites are due to the coexistence of multiple final states after electron transfer from Mn to surrounding O ligands. In addition, the Mn $2p_{3/2}$ (Mn $2p_{1/2}$) main line presents a fine structure showing two peaks C and D (C′ and D′) 1.2 eV apart from each other. Note that feature D in the Mn $2p_{3/2}$ peak is more intense than feature C. Further annealing to 800 K led to a slight modification of the Mn 2p line shapes: the fine structure observed in the Mn $2p_{3/2}$ cannot be resolved anymore and the lines become slightly narrower and apparently shifted toward higher binding energy. The overall shape of the Mn 2p spectra obtained after annealing is characteristic of Mn^{2+}.[15−20] The slight modifications of the Mn 2p fine structure (C, D, C′, and D′) after the final annealing will be addressed in detail in a separate study involving charge transfer multiplet calculations as well as X-ray absorption near edge structure (XANES) analysis.[21] In the present system, Mn^{2+} can be expected inside a rocksalt MnO segregated phase or in wurtzitic (Zn,Mn)O where Mn atoms substitute Zn in the ZnO lattice, but the conclusions of this separate study suggest that these spectral modifications are related to the existence of traces of additional phases for the annealing steps at the lowest temperature rather than a change in the crystal field symmetry.

3.2. Stoichiometry and Mn Diffusion. Lumping all the technical aspects of a photoemission experiment (geometry of the setup, transmission of the analyzer, photon energy, etc.) together as a constant, the intensity of the photoelectron signal related to a given subshell from a specific element B homogeneously distributed inside a material A follows:

$$I_{B,A} \propto \sigma_B \lambda_{B,A} C_{B,A} \qquad (1)$$

where σ is the photoemission cross section of the subshell, λ is IMFP (if elastic scattering effects are neglected[22]), and C is the atomic concentration of the specific element in the material. When B is included into two different materials A and C, the ratio of the XPS intensity related to the subshell of B into these two materials is given by

$$\frac{I_{B,A}}{I_{B,C}} = \frac{\lambda_{B,A} C_{B,A}}{\lambda_{B,C} C_{B,C}} \qquad (2)$$

provided experimental conditions are otherwise identical.

This relationship will be used in the following for interpreting variations in the core level intensities of the Mn 2p, Zn 3s, and O 1s lines with respect to Mn deposition, oxidation, and diffusion. IMFP values are estimated using the so-called TPP-2 M formula.[24] The values of all parameters required for the following simulations are summarized in Table 1.

In Figure 2, we show the HAXPES intensity of the Mn 2p, Zn 3s, and O 1s lines at various steps of the experiment. The Zn 3s peak was preferred to Zn 2p as the zinc-related signal, because Zn 2p was not recorded under the same experimental conditions as Mn 2p, Zn 3s, and O 1s (the monochromator slit had to be reduced to compensate for the intensity of the Zn 2p line). The HAXPES intensity is normalized to the intensity of the incident

Table 1. Parameters Used for Calculating the IMFP λ in Three Materials

	ZnO	MnO	Mn
lattice Structure	wurtzite	wurtzite	cubic
a (nm)	0.325	0.3314	8.91
c (nm)	0.521	0.5412	
density (kg/m³)	5.606	4.588	7.470
molar mass (kg/mol)	81.389×10^{-3}	70.938×10^{-3}	54.938×10^{-3}
band gap (eV)	3.4	3.6^b	
$N_v{}^a$	18	13	7
$C_{Mn,XO}(z,t)$ [Mn or Zn] (atoms/m³)	4.14×10^{28}	3.89×10^{28}	8.19×10^{28}
$\lambda_{Mn2p,\ 2859\ eV}$ (nm)	4.702	4.556	3.821
$\lambda_{Zn3s,\ 3362\ eV}$ (nm)	5.198	5.367	4.356

^{a} N_v is the number of valence electron per ZnO or MnO molecule, required for the TPP-2M formula.[24] ^{b} The band gap of wurtzite MnO is not known. Therefore, we used the value from rocksalt MnO.[23]
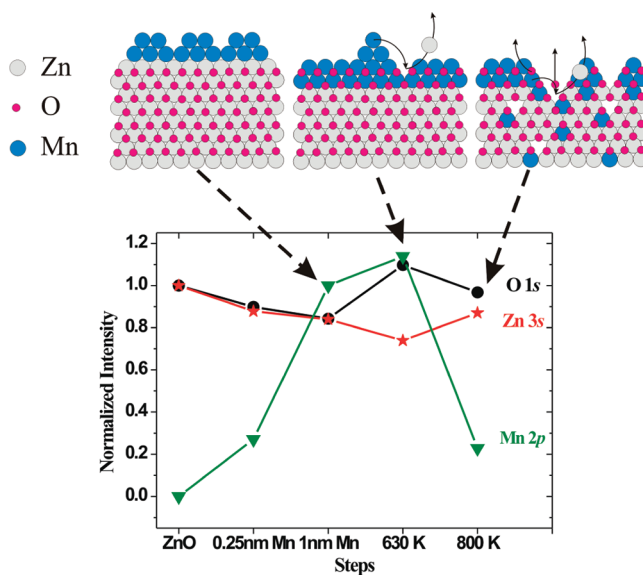

Figure 2. Integrated HAXPES intensity of the Mn 2p, Zn 3s, and O 1s lines at the successive steps of the experiment: bare ZnO surface, Mn deposition (two steps: 0.25 nm and additional 0.75 nm), and two annealing steps (at 630 and 800 K, 25 min each step). Drawings are added to the graph in order to illustrate the physicochemical phenomena reported at each step and described in detail in the text.

beam and the data acquisition time. The Mn 2p signal was recorded from the 1 nm as-grown Mn coverage and the Zn 3s and O1s signal intensities from the clean ZnO surface are set to unity.

As seen in Figure 2, both the O 1s and Zn 3s signals are attenuated upon Mn deposition (in two steps). The intensity $I_{0,A}$ of XPES signals from a bulk material A is attenuated by a layer of material B of thickness d so that the recorded intensity becomes

$$I_A = I_{0,A}\ e^{-d/\lambda_B} \qquad (3)$$

The attenuation of these signals can therefore be used to verify the thickness d_{Mn} of the deposited Mn. A thickness d_{Mn} of 0.8 nm was calculated based on the attenuation of the Zn 3s signal. This value is slightly smaller than the value of 1 nm estimated using the

quartz thickness monitor but constitutes the lower limit of the amount of Mn deposited. Indeed this calculation is based on the hypothesis that the Mn film is growing layer by layer, that is, two-dimensionally. A larger Mn amount is required to achieve the same attenuation if the film is instead growing three-dimensionally, which is very likely the case according to the literature.[25]

At 630 K, we observed an increase in the intensity of the oxygen peak with respect to the zinc. From Figure 1, it is seen that these phenomena occur simultaneously with Mn oxidation. We can thus conclude that Mn oxidation proceeds via Zn substitution, with the substituted zinc being sublimated. The vapor pressure of elemental Zn is indeed very high at this temperature ($P_{vap,Zn}^{630K} \sim 1 \times 10^{-2}$ mbar). Again, the thickness of the MnO film can be estimated from the attenuation of the Zn 3s signal. A value of $d_{MnO} \sim 1.6$ nm was calculated from eq 3. Owing to the respective structural properties of the wurtzite MnO layer and the as-grown Mn film, these values d_{MnO} and d_{Mn} correspond to the same area density of 6.6×10^{19} Mn atoms/m². This estimate is based on the assumption that the MnO layer is formed by Zn substitution. Hence, the wurtzite structure of ZnO was imposed on MnO which usually appears in rocksalt (rs) structure. The structural parameters of wurtzite MnO are very close to those from ZnO and were taken from Schrön et al.[26]

The increase in intensity of Mn 2p upon oxidation of Mn has probably two origins. First, with XPS being a surface-sensitive technique, the signal emitted from a given amount of material grown as a thin film on a substrate is larger if the structure of the film is two-dimensional (2D) and spreads over the whole substrate area and is smaller if, instead, the film is three-dimensional (3D) and covers a fraction of the surface. As we mentioned earlier, the structure of the metallic Mn layer initially grows as a three-dimensional film while oxidation proceeds via Zn substitution from a very flat substrate (obtained by MCP polishing; see refs 27 and 28) and leads to the formation of a 2D MnO layer. Thanks to eq 2 and owing to the fact that the XPS intensity from a thin film of thickness d follows

$$I = I_0 \left(1 - e^{-d/\lambda}\right) \qquad (4)$$

where I_0 is the intensity from an infinitely thick layer, we calculated the intensity variation from a 3D Mn film and a 2D MnO layer. As a matter of fact, we could not reproduce the increase from 1 to 1.14 of the Mn 2p XPS intensity upon annealing at 630 K. Actually, it is highly probable that this variation is also partly due to the difficulty of comparing the area of Mn 2p peaks before and after oxidation. Indeed, the shape of the peak and the background change dramatically between these two steps (see Figure 1), and obtaining an absolute value of the Mn 2p area with an error smaller than 10% is probably impossible.

Upon annealing at 800 K, the signal from Mn 2p drops considerably and the Zn:O stoichiometry of 1:1 is almost restored. According to Kleinlein and Helbig,[29] Mn diffuses into the bulk of ZnO, which explains the intensity loss. We exclude re-evaporation of Mn atoms as the heat of formation of manganese oxide (between −350 and −400 kJ/mol) is smaller than that of ZnO (−300 to −350 kJ/mol), which means that MnO is more stable than ZnO.[12] As seen previously, a 2D MnO film is formed on the surface prior to this last annealing step. Hence, diffusion of Mn deeper into the bulk of ZnO requires the decomposition of this surface oxide. The excess of O is then released, which partially restores the stoichiometry of ZnO.
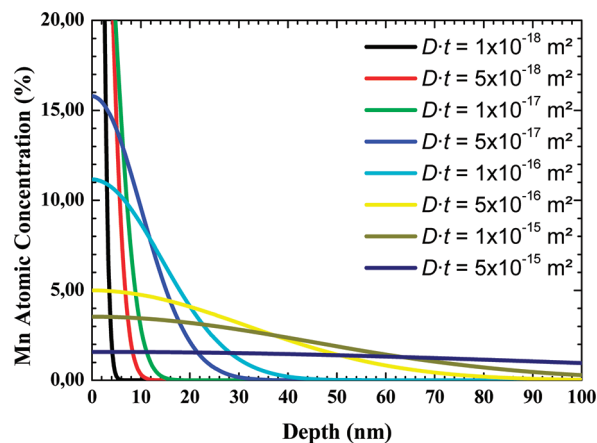

Figure 3. Atomic concentration profiles for Mn diffusion into ZnO. Calculation based on Fick's second law (eq 5) for various values of Dt. The initial Mn area density was estimated to be 6.6×10^{19} atoms/m², and $C_{B,A}(z,t)$ was divided by the molecular density of ZnO (4.14×10^{28} molecules/m³) in order to present $C_{B,A}(z,t)$ as atomic concentrations.

The diffusion of Mn from a thin, almost pure 2D MnO film into the bulk of ZnO can be described by Fick's second law:

$$C_{B,A}(z,t) = \frac{Q}{\sqrt{\pi Dt}} \, e^{-z^2/4Dt} \qquad (5)$$

where z is the coordinate normal to the surface, t is the annealing/diffusion time, and D (m²/s) is the temperature-dependent diffusion coefficient for material B into material A. For the sake of simplicity, we will not separate the various diffusion channels (substitutional diffusion, grain diffusion, etc.). Q is the initial amount (number of atoms/m²) of Mn in the 2D MnO film which was estimated above to be about 6.6×10^{19} atoms/m². Figure 3 shows such depth profiles calculated for various values of Dt.

The only unknown parameter in eq 5 is the Mn diffusion coefficient D. In the following, we will estimate $C_{B,A}(z,t)$ and hence D from the attenuation of the Mn 2p XPS signal, which is dependent on the distribution profile of the Mn atoms upon annealing at 800 K. In order to achieve this, we must express $I_{B,A}$ as a sum of signals $I_{B,A,\Delta z}$ emitted from thin layers of thickness $\Delta z = c/2$ ($c = 0.52$ nm for ZnO) and located at increasing depth with respect to the surface of the material.

$$I_{B,A} = \sum_{n=0}^{\infty} \left[\left(C_{B,A}(z,t) \, I_{B,A,\Delta z}(z)\right) e^{-n\Delta z/\lambda} \right] \qquad (6)$$

with $I_{B,A,\Delta z}$ given by eq 4 for a layer of thickness Δz. Finally, according to eqs 2, 4, and 6, we can estimate the intensity ratio between the Mn 2p signals prior and after annealing:

$$\frac{I_{Mn,ZnO}}{I_{Mn,MnO}} = \frac{\lambda_{ZnO}}{\lambda_{MnO}} \frac{\sum_{n=0}^{\infty} \left\{ \left[C_{Mn,ZnO}(z,t) \left(1 - e^{\Delta z/\lambda_{ZnO}}\right) \right] e^{-n\Delta z/\lambda} \right\}}{C_{Mn,MnO}\left(1 - e^{d_{MnO}/\lambda_{MnO}}\right)}$$

$$(7)$$

From the values of d_{MnO} calculated above and from those of $C_{Mn,MnO}(z,t)$ and λ_{MnO} in Table 1, we can estimate the denominator of eq 7; the numerator is calculated numerically by adding intensities emitted by successive ZnO double layers ($\Delta z \sim 0.26$ nm) at increasing depth inside the ZnO single crystal. Figure 4a shows the results corresponding to the diffusion
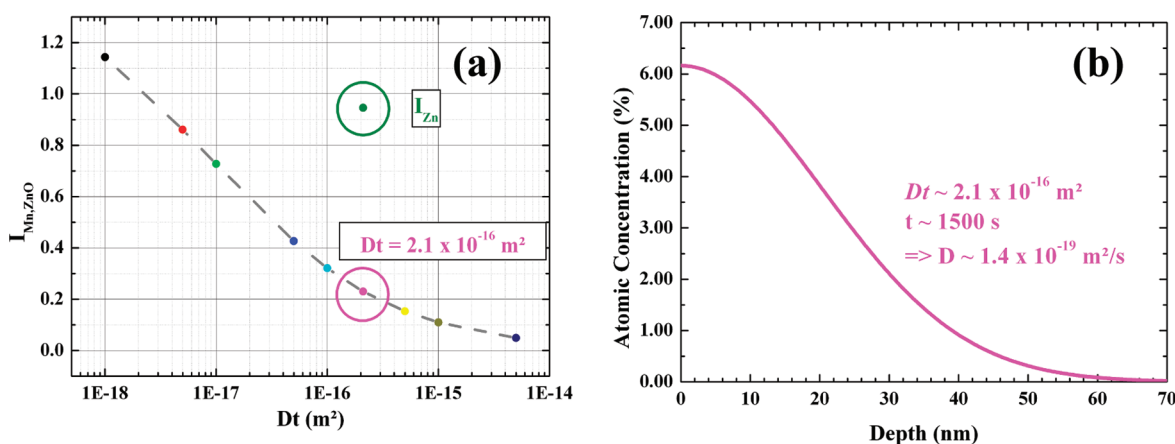
20606

dx.doi.org/10.1021/jp206075w |J. Phys. Chem. C 2011, 115, 20603–20609

Figure 4. (a) Calculated Mn 2p HAXPES intensity versus Dt for the various Mn atomic concentration profiles shown in Figure 3. An additional value was calculated for $Dt = 2.1 \times 10^{-16}$ m^2, corresponding to the diffusion profile shown in (b) and to an XPS intensity comparable to that measured after annealing at 800 K. The Zn 3s intensity corresponding to $Dt = 2.1 \times 10^{-16}$ m^2 is also shown in (a); see text for more details.

profiles shown in Figure 3. According to eq 7, the results were multiplied by $I_{Mn,MnO}$ (∼1.14, see Figure 2).

The curve in Figure 4a illustrates that a value of Dt near 2.1×10^{-16} m^2 agrees best with to the intensity drop of the Mn 2p signal from 1.14 to 0.23 upon annealing. From the annealing time, 1500 s, we can deduce that the overall diffusion coefficient of Mn into ZnO at 800 K is approximately 1.4×10^{19} m^2/s. We are not aware of the diffusion coefficient of Mn into ZnO in the temperature range around 800 K, and an Arrhenius-type extrapolation of data recorded between 1400 and 1600 K by Kleinlein and Helbig[29] results in a value many orders of magnitude below our value of D. Nevertheless, a similar conclusion was recently reached by Koskelo et al.,[30] namely that their diffusion coefficients D for the diffusion of Co into ZnO were several orders of magnitude above that from Kleinlein and Helbig. In fact, considering Koskelo et al.'s results, it seems that the diffusion coefficient extracted from our data is of the same order of magnitude as for the substitutional diffusion of other elements such as Cu, In, and Co in ZnO. This conclusion is in fair agreement with the fact that, as shown above, Zn substitution by Mn proceeds during the oxidation process.

Finally it is also worth mentioning that, as shown in Figure 4a, the intensity of the Zn 3s signal calculated from the diffusion profile for $Dt \sim 2.1 \times 10^{-16}$ m^2 (leading to $I_{Mn,ZnO} \sim 0.23$) is slightly larger than the experimental value ($I_{Mn,ZnO} \sim 0.87$, see Figure 2). This can easily be explained by the creation of Zn vacancies after the diffusion of Mn deeper into the material. This hypothesis is supported by the slight O excess remaining after the final annealing (Figure 2).

3.3. Band Bending. The bending of electronic bands at semiconductor surfaces or interfaces lies in the respective position of the Fermi level (E_F) and of the charge neutrality level (CNL). While E_F is mostly determined by doping, the CNL is an intrinsic property of the material related to the presence of a continuum of virtual gap states (VIGS) at semiconductor surfaces or interfaces as a result from the broken bulk symmetry.[31] In addition, King et al.[32] have recently shown that the position of the CNL also dictates the electrical behavior of defects and hence coincides with the Fermi level stabilization energy (E_{FS}) defined by Walukiewicz in his so-called amphoteric defect model (ADM) level.[33] Hence, if large amounts of defects or impurities are introduced in a semiconductor, the Fermi level

will converge toward the CNL. These two pieces of information are important for understanding the present results.

In the present work, we have access to several data which allow us to describe the alignment of the energy bands at the various stages of the experiment properly. The relative energy shifts of the Zn and O core levels from a given experimental step to the other indicate band bending. The leading edge of the valence band indicates the position of the Fermi level within the energy gaps (if any) of the materials. Finally, according to the preceding sections, we know the oxidation states of Mn and Zn and we can then refer to the literature regarding the intrinsic properties of the materials such as electroaffinity (for semiconductors) or work function (for metals), band gap, and so forth.

As seen in Figure 5a, the valence band of the bare ZnO surface is located 3.4 eV below the Fermi level which coincides with the conduction band minimum (CBM) as illustrated in Figure 5c. This is typical of ZnO[34,35] and has its origin in the fact that the CNL of ZnO is located ∼0.2 eV above the CBM[36] and that ZnO is highly reactive to hydrogen, a very shallow donor impurity of ZnO.[37,38] Hence, the inevitable presence of hydrogen lifts the Fermi level close the CNL. If H is present at the surface only, the energy band must bend downward in the vicinity of the surface. If H is present deeper in the bulk of the material, the bands should be flat. The presence of hydroxide compounds is not seen in the O 1s spectra of the bare ZnO surface (Figure 1) while the (1×1) LEED pattern is typical of a hydrogenated ZnO $(000\bar{1})$ surface.[39] This contradiction can be attributed to the poorer surface sensitivity of HAXPES (compared to usual XPS). In addition to the adsorption of H at the surface, bulk H might also be present. As explained above, the surface preparation of ZnO involves annealing at 875 K. At such a temperature, interstitial H atoms bound to O (H_i) should all be diffused out of the material. Nevertheless, H might still be present at O vacancy sites (H_O) where it would not be detectable in the O related XPS lines. Actually, there is still a controversy on the thermal stability of H_O: while some reports mention the complete desorption of H from H_O sites around 800 K for H* or ^{2}H* plasma-treated samples,[40] an activation barrier as high as 1.7 eV was calculated[41] for the diffusion of H_O and a strong hydrogen desorption was recorded on ZnO samples annealed above 1100 K.[42,43] This all means that, depending on the sample growth conditions, substantial amounts of H_O may be present in ZnO
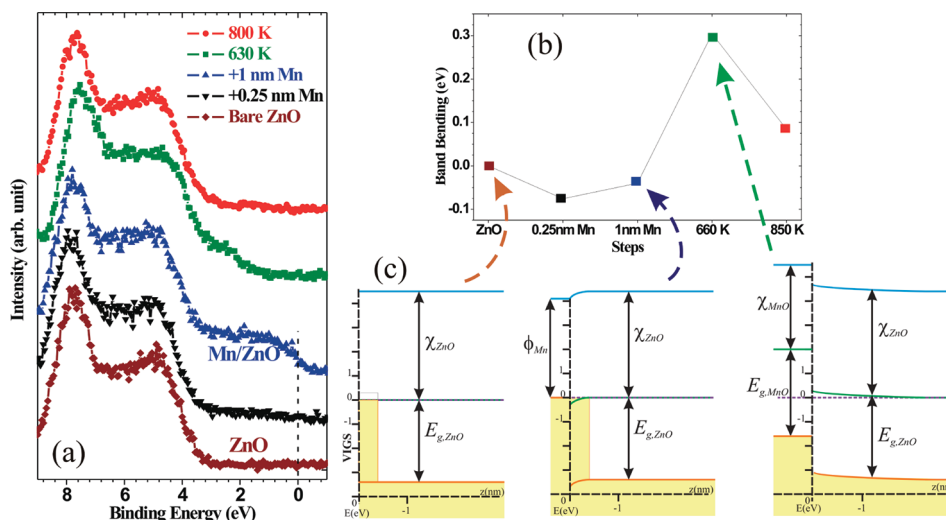
Figure 5. (a) Valence band of Mn/ZnO at different stages of the experiment. (b) Band bending measured by the binding energy shifts of Zn 2p with respect to the Fermi level. Negative values correspond to an upward band bending. (c) Energy band alignment after Mn deposition (middle panel) and oxidation (right panel).

and thermally stable even at 875 K, the highest temperature reached during our sample preparation. Hence, we believe that, in the present case, there is a bulk hydrogen contamination and hence a flat band situation (Figure 5c).

A steep downward bending of ZnO bands is observed upon Mn deposition (Figure 1). Such band bending is not seen in Figure 5b which only refers the displacements of the main Zn and O components. Indeed, as said above and pictured in Figure 5c, this band bending is confined at the Mn/ZnO interface and the XPES spectra are still dominated by the bulk, non shifted components. The band bending can easily be related to the mismatch between the work function of Mn (ϕ_{Mn} = 4.1 eV for polycrystalline Mn) and the CNL of ZnO. The confinement is explained by the very localized nature of VIGS in real space leading to the formation of accumulation layers at the ZnO $(000\bar{1})$ surface, which can even show quantized electron sub-band states.[36,44]

Upon annealing, a thin MnO film forms on top of the surface of ZnO. As seen in Figure 5a, the valence band edge appears at a binding energy roughly 1 eV above that of ZnO. According to the literature,[45] this feature can be attributed to hybrid O 2p—Mn 3d antibonding states which are predicted to be the highest occupied states in MnO. In the present work, the valence band edge of MnO is located around ~1.6 eV below the Fermi edge, which is also 0.8 eV further away than typical valence band onset values reported in the literature.[46] As seen in Figure 5a and b, the ZnO bands moves 0.3 eV closer to the Fermi level. In the present case, the band bending is seen as a displacement of Zn and O related XPS spectral features. No more bulk (flat band) related feature is seen in the spectra related to ZnO. Owing to the respective band gaps and electroaffinities from MnO and ZnO,[47] a band discontinuity appears at the interface between the two oxides (Figure 5c). As the Fermi level moves away from the CNL of ZnO, we must assume that the charge transfer between MnO and ZnO is insufficient to reach a situation where the CNL of both ZnO and MnO coincides with the Fermi level. As illustrated in Figure 5c (right panel), this means that, upon Mn oxidation, the ZnO substrate underneath is no more terminated by a highly conductive layer and hence band bending extends much further into the bulk of ZnO.

Finally, upon dilution, the local concentration of Mn drops down to a few percent. The band structure of (Zn,Mn)O becomes very close to that of ZnO. We also observe that Mn does not dope ZnO, or in other words that the incorporated Mn in a 2+ state does not modify the position of the Fermi level within the band gap of ZnO.

4. CONCLUSIONS

A detailed analysis of the physical processes and chemical reactions (charge transfer, formation of a two-dimensional MnO layer, and Mn diffusion occurring at the Mn/ZnO interface) has been provided thanks to the bulk-sensitivity of HAXPES. Charge transfer occurs between the metallic Mn film and the ZnO surface and causes the downward band bending of the ZnO valence band in the interfacial region. Oxidation and diffusion of a thin Mn film grown onto ZnO $(000\bar{1})$ upon annealing leads to various side effects which may play a crucial role in nanometer-scale devices. In particular, we identified a modification of the band bending and conductivity at the Mn/ZnO interface upon annealing. It was found that Mn diffuses via substitution in ZnO, and the related diffusion coefficient was experimentally determined ($Dt \sim 1.4 \times 10^{-19}$ m^2/s).

■ AUTHOR INFORMATION

Corresponding Author
*E-mail: mugumaom@fundp.ac.be.; mugcubaka@gmail.com.

■ REFERENCES

(1) Fadley, C. S. *Surf. Interface Anal.* **2008**, *40*, 1579–1605.

(2) Drube, W. *Nucl. Instrum. Methods Phys. Res., Sect. A* **2005**, *547*, 87–97.

(3) Theodoropoulou, N.; Misra, V.; Philip, J.; LeClair, P.; Berera, G. P.; Moodera, J. S.; Satpati, B.; Som, T. *J. Magn. Magn. Mater.* **2006**, *300*, 407–411.

(4) Ueda, K.; Tabata, H.; Kawai, T. *Appl. Phys. Lett.* **2001**, *79*, 988–990.

(5) Pan, F.; Song, C.; Liu, X. J.; Yang, Y. C.; Zeng, F. *Mater. Sci. Eng., R* **2008**, *62*, 1–35.

(6) Coey, J. M. D.; Chambers, S. A. *MRS Bull.* **2008**, *33*, 1053–1058.

(7) Droubay, T. C.; Keavney, D. J.; Kaspar, T. C.; Heald, S. M.; Wang, C. M.; Johnson, C. A.; Whitaker, K. M.; Gamelin, D. R.; Chambers, S. A. *Phys. Rev. B* **2009**, *79*, 155203, 9 pp.

(8) Zou, C. W.; Wu, Y. Y.; Sun, B.; Gao, W.; Xu, P. S. *Surf. Interface Anal.* **2007**, *39*, 865–870.

(9) Guziewicz, E.; Kopalko, K.; Sadowski, J.; Guziewicz, M.; Golacki, Z.; Kanski, J.; Ilver, L. *Phys. Scr., T* **2005**, *115*, 541–544.

(10) Grossner, U.; Gabrielsen, S.; Børseth, T. M; Grillenberger, J.; Kuznetsov, A. Yu.; Svensson, B. G. *Appl. Phys. Lett.* **2004**, *85*, 2259–2261.

(11) Wang, X. D.; Summers, C. J.; Wang, Z. L. *Appl. Phys. Lett.* **2005**, *86*, 013111, 3 pp.

(12) Campbell, C. T. *Surf. Sci. Rep.* **1997**, *27*, 1–111.

(13) Sumiya, M.; Lozach, M.; Matsuki, N.; Ito, S.; Ohashi, N.; Sakoda, K.; Yoshikawa, H.; Ueda, S.; Kobayashi, K. *Phys. Status Solidi C* **2010**, *7*, 1903–1905.

(14) Oku, M.; Hirokawa, K.; Ikeda, S. *J. Electron Spectrosc. Relat. Phenom.* **1975**, *7*, 465–473.

(15) van Elp, J.; Potze, R. H.; Eskes, H.; Berger, R.; Sawatzky, G. A. *Phys. Rev. B* **1991**, *44*, 1530–1537.

(16) Allegretti, F.; Franchini, C.; Bayer, V.; Leitner, M.; Parteder, G.; Xu, B.; Fleming, A.; Ramsey, M. G.; Podloucky, R.; Surnev, S.; Netzer, F. P. *Phys. Rev. B* **2007**, *75*, 224120, 8 pp.

(17) Oku, M.; Wagatsuma, K.; Konishi, T. *J. Electron Spectrosc. Relat. Phenom.* **1999**, *98−99*, 277–285.

(18) Mizokawa, T.; Nambu, T.; Fujimori, A.; Fukumura, T.; Kawasaki, M. *Phys. Rev. B* **2002**, *65*, 085209, 8 pp.

(19) Parmigiani, F.; Sangaletti, L. *J. Electron Spectrosc. Relat. Phenom.* **1999**, *98−99*, 287–302.

(20) Müller, F.; de Masi, R.; Reinicke, D.; Steiner, P.; Hüfner, S.; Stöwe, K. *Surf. Sci.* **2002**, *520*, 158–172.

(21) Mugumaoderha, M. C.; Sporken, R.; Ghijsen, J.; de Groot, F. M. F.; Dumont, J. A. *J. Phys. Chem. C*, submitted.

(22) Jablonski, A.; Powell, C. J. *J. Electron Spectrosc. Relat. Phenom.* **1999**, *100*, 137–160.

(23) Anisimov, V. I.; Korotin, M. A.; Kurmaev, E. Z. *J. Phys.: Condens. Matter* **1990**, *2*, 3973–3987.

(24) Tanuma, S.; Powell, C. J.; Penn, D. R. *Surf. Interface Anal.* **2003**, *35*, 268–275.

(25) Baümer, M.; Freund, H. J. *Prog. Surf. Sci.* **1999**, *61*, 127–198.

(26) Schrön, A.; Rödl, C.; Bechstedt, F. *Phys. Rev. B* **2010**, *82*, 165109, 12 pp.

(27) Dumont, J.; Couet, S.; Seldrum, T.; Moisson, C.; Turover, D.; Sporken, R. *J. Vac. Sci. Technol., B* **2006**, *24*, 2124–2131.

(28) Dumont, J.; Mugumaoderha, M. C.; Seldrum, T.; Frising, F.; Moisson, C.; Turover, D.; Sporken, R. *J. Vac. Sci. Technol., B* **2007**, *25*, 1536–1541.

(29) Kleinlein, F. W.; Helbig, R. *Z. Phys. A* **1974**, *266*, 201–207.

(30) Koskelo, O.; Räisänen, J.; Tuomisto, F.; Eversheim, D.; Grasza, K.; Mycielski, A. *Thin Solid Films* **2010**, *518*, 3894–3897.

(31) Mönch, W. *Appl. Surf. Sci.* **1997**, *117−118*, 380–387.

(32) King, P. D. C.; Veal, T. D.; Jefferson, P. H.; Zúñiga-Pérez, J.; Muñoz-Sanjosé, V.; McConville, C. F. *Phys. Rev. B* **2009**, *79*, 035203, 5 pp.

(33) Walukiewicz, W. *Phys. B* **2001**, *302−303*, 123–134.

(34) Ashrafi, A. *Surf. Sci.* **2010**, *604*, L63–L66.

(35) Girard, R. T.; Tjernberg, O.; Chiaia, G.; Söderholm, S.; Karlsson, U. O.; Wigren, C.; Nylén, H.; Lindau, I. *Surf. Sci.* **1997**, *373*, 409–417.

(36) Piper, L. F. J.; Preston, A. R. H.; Fedorov, A.; Cho, S. W.; DeMasi, A.; Smith, K. E. *Phys. Rev. B* **2010**, *81*, 233305, 4 pp.

(37) Lavrov, E. V. *Phys. B* **2009**, *404*, 5075–5079.

(38) Janotti, A.; Van de Walle, C. G. *Rep. Prog. Phys.* **2009**, *72*, 126501, 29 pp.

(39) Kunat, M.; Gil Girol, S.; Becker, T.; Burghaus, U.; Wöll, Ch. *Phys. Rev. B* **2002**, *66*, 081402, 8 pp.

(40) Ip, K.; Overberg, M. E.; Heo, Y. W.; Norton, D. P.; Pearton, S. J.; Stutz, C. E.; Kucheyev, S. O.; Jagadish, C.; Williams, J. S.; Luo, B.; Ren, F.; Look, D. C.; Zavada, J. M. *Solid-State Electron.* **2003**, *47*, 2255–2259.

(41) Bang, J.; Chang, K. J. *J. Korean Phys. Soc.* **2009**, *55*, 98–102.

(42) Weber, M. H.; Lynn, K. G. *J. Phys.: Conf. Ser.* **2011**, *262*, 012063, 6 pp.

(43) Nickel, N. H. *Superlattices Microstruct.* **2007**, *42*, 3–7.

(44) Dumont, J.; Hackens, B.; Faniel, S.; Mouthuy, P. O.; Sporken, R.; Melinte, S. *Appl. Phys. Lett.* **2009**, *95*, 132102, 3 pp.

(45) Massidda, S.; Continenza, A.; Posternak, M.; Baldereschi, A. *Phys. Rev. Lett.* **1995**, *74*, 2323–2326.

(46) Nagel, M.; Biswas, I.; Nagel, P.; Pellegrin, E.; Schuppler, S.; Peisert, H.; Chassé, T. *Phys. Rev. B* **2007**, *75*, 195426, 6 pp.

(47) Xu, Y.; Schoonen, M. A. A. *Am. Mineral.* **2000**, *85*, 543–556.

20609

dx.doi.org/10.1021/jp206075w |*J. Phys. Chem. C* 2011, 115, 20603–20609